Energy & Environmental Science

ROYAL SOCIETY OF CHEMISTRY

PAPER

View Article Online
View Journal | View Issue

Cite this: *Energy Environ. Sci.*, 2022, **15**, 4636

A high-rate and high-efficiency molten-salt sodium–oxygen battery†

Yun Guang Zhu, [ab] Graham Leverick, *[ac] Alessandra Accogli, [ad] Kiarash Gordiz, [ac] Yirui Zhang [ac] and Yang Shao-Horn *[abce]

Received 3rd June 2022,
Accepted 16th September 2022

DOI: 10.1039/d2ee01774a

rsc.li/ees

Alkali metal–oxygen batteries can provide greater specific energy than Li-ion batteries but often suffer from low power density, cycleability, and energy efficiency due to the sluggish kinetics of the oxygen electrode and parasitic reactions at both the oxygen and alkali metal electrodes. In this study, we demonstrated a molten-salt Na–O_2 battery operating at 443 K with high areal energy (33 mW h cm^{-2}_{geo}) and power densities (19 mW cm^{-2}_{geo}), with high energy efficiency (~90% at 5 mA cm^{-2}_{geo}), and stable cycling (400 cycles with no capacity loss). Raman, pressure tracking and titration measurements were used to show that the dominant discharge product is Na_2O_2. Moreover, the redox activity of nitrate anions in the molten salt was found to be critical to enable the formation of Na_2O_2. Through ^{18}O-labeling experiments as well as discharging Na–Ar cells, we demonstrated that the discharge reaction occurs *via* the electrochemical reduction of $NaNO_3$ to Na_2O and $NaNO_2$, where chemical reactions with O_2 lead to the formation of Na_2O_2 from Na_2O, and the regeneration of $NaNO_3$ from $NaNO_2$.

Broader context

Alkali metal–oxygen batteries have high theoretical energy densities and are promising electrochemical energy storage systems to enable the electrification of heavy-duty vehicles and aviation. Unfortunately, the practical realization of such metal–oxygen batteries is hindered by low power density, cycleability, and energy efficiency due to slow reacitons in the oxygen electrode and unwanted side reactions in both the oxygen and alkali metal electrodes. In this study, we introduce a novel molten-salt Na–O_2 battery which operates at 170 °C featuring a liquid sodium metal negative electrode and Nickel-based oxygen electrode with a molten-salt electrolyte. By operating at increased temperature and using catalytically active nickel in the oxygen electrode, the rate capability of the battery is significantly enhanced. Moreover, the molten-salt electrolyte shows high stability; reducing parasitic reactions and enhancing cycle life.

Introduction

Alkali metal–oxygen batteries have high theoretical energy densities and are promising electrochemical energy storage systems to enable the electrification of heavy-duty vehicles and aviation.[1] For instance, Li–, Na–, and K–O_2 batteries can deliver values of specific energy of 3458 W h kg^{-1} (Li, O_2/active Li_2O_2), 1103 W h kg^{-1} (Na, O_2/active NaO_2), and 935 W h kg^{-1} (K, O_2/active KO_2) at room temperature, respectively (where calculation details can be found in the ESI†). However, the formation of dendrites[2] and the high reactivity of alkali metals has hindered the development of metal-based batteries, including metal–oxygen batteries.[3] Recently, research effort has focused on modifying the alkali metal negative electrode to increase rechargeability and stability, especially that of lithium metal.[4,5] Moreover, the sluggish kinetics of the oxygen reduction and evolution reactions (ORR and OER)[6] and slow diffusion of oxygen in the air electrode[7] can increase the overpotentials at the positive electrode of metal–oxygen batteries, leading to poor energy efficiencies.[8,9] To reduce the overpotentials of metal–oxygen batteries, solid electrochemical catalysts[10] and redox mediators[11,12] have been intensely investigated. Unfortunately, the (electro)chemical stability of the electrodes[13] and electrolyte[14–16] against reaction intermediates and products as well as the operating voltages remain a big challenge.

Recently, a molten-salt Li–O_2 battery has been reported by Giordani *et al.* in 2016, showing high electrolyte stability and

Electrochemical Energy Laboratory, Massachusetts Institute of Technology, Cambridge, MA, USA. E-mail: shaohorn@mit.edu, leverick@mit.edu
[b] *Research Laboratory of Electronics, Massachusetts Institute of Technology, Cambridge, MA, USA*
[c] *Department of Mechanical Engineering, Massachusetts Institute of Technology, Cambridge, MA, USA*
[d] *Dipartimento di Chimica, Materiali e Ingegneria Chimica Giulio Natta, Politecnico di Milano, 20131, Milano, Italy*
[e] *Department of Material Science, Massachusetts Institute of Technology, Cambridge, MA, USA*

† Electronic supplementary information (ESI) available. See DOI: https://doi.org/10.1039/d2ee01774a

high-energy efficiency (~95%) at an operating temperature of 423 K.[17] Unfortunately, the formation of Li_2CO_3 from the oxidation of carbon in the oxygen electrode led to poor cycling stability (<50 cycles, ~2.6 mA h cm^{-2}_{geo} at ~0.6 mA cm^{-2}_{geo}, normalized based on the geometric area of the positive electrode). Subsequently, Xia *et al.* have demonstrated a molten-salt Li–O_2 battery with a four-electron conversion of O_2 to Li_2O using NiO in the oxygen electrode, showing stable cycling performance (150 cycles, 0.5 mA h cm^{-2}_{geo} at 0.2 mA cm^{-2}_{geo}) with a Coulombic efficiency of ~100%.[18] Koo and Kang have reported that iron(II, III) oxide can also serve as an effective catalyst to produce Li_2O in nitrate molten-salt Li–O_2 batteries.[19] Most recently, we have shown that Li_2O in nitrate molten-salt Li–O_2 batteries is enabled by the redox activity of nitrate anions and by studying different 3d transition metal oxides have found that NiO has the lowest overpotential during discharge due to its optimal binding of nitrate and nitrite anions.[20] Nitrate molten salts have also been used as the O_2 reservoir for a closed Li–O_2 battery system[21] and molten-salt electrolytes have been used with other metal–oxygen batteries besides Li such as Fe,[22,23] Zn[24] and Mg,[25] showing long cycling life and high rate capability. A schematic of the structure of a molten-salt Li–O_2 battery is shown in Fig. 1a. Solid-state electrolytes are needed in molten-salt Li–O_2 batteries to prevent crossover of soluble Li_2O that can form due to the reaction between Li metal and the electrolyte.[26] A molten-salt buffer layer was used to provide a highly Li^+ conducting interface between the Li metal electrode and solid-state electrolyte in order to achieve high rate and energy efficiency in molten-salt Li–O_2 batteries. Replacing Li by Na provides an opportunity to increase the power of the system due to low interfacial resistance between liquid Na and the solid-state electrolyte at an operating temperature of 443 K.

In this work, a molten-salt Na–O_2 battery was developed with a liquid Na negative electrode and Ni oxygen electrode with a $NaNO_3$/KNO_3/$CsNO_3$ eutectic salt electrolyte and a β-Al_2O_3 membrane, where the stable interface between liquid Na and β-Al_2O_3 can be advantageous relative to molten-salt Li–O_2 batteries[27] (Fig. 1b). Such molten-salt Na–O_2 batteries showed high energy (33 mW h cm^{-2}_{geo}) and power densities (19 mW cm^{-2}_{geo}) as well as stable cycling (400 cycles, 0.5 mA h cm^{-2}_{geo} at 5 mA cm^{-2}_{geo}). Using Raman, pressure tracking and titration measurements, we show that the dominant discharge product is Na_2O_2. Moreover, the redox of nitrate anions is identified as being critical to enable the formation of Na_2O_2 upon discharge. Molten-salt Na–Ar cells show the electrochemical reduction of $NaNO_3$ to Na_2O and $NaNO_2$. On the other hand, in an O_2 environment the formed Na_2O and $NaNO_2$ can further react with O_2 to yield Na_2O_2 and regenerate $NaNO_3$, respectively. Finally, using ^{18}O-labeling experiments, we demonstrate that the oxygen reduction reaction in molten-salt Na–O_2 batteries occurs *via* a nitrate-mediated mechanism whereby $NaNO_3$ facilitates an apparent $2e^-/O_2$ overall reaction to form Na_2O_2. The presented nitrate-mediated molten-salt Na–O_2 battery provides a novel approach to develop alkali metal–O_2 batteries with high energy and power densities, with a cell architecture that can stabilize the alkali metal electrode.

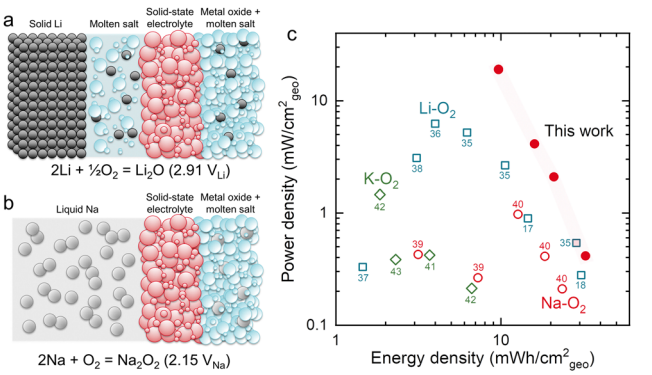

Fig. 1 Schematic of a molten-salt Li–O_2 battery[18] (a) and the molten-salt Na–O_2 battery demonstrated in this work (b). A conventional molten-salt Li–O_2 battery contains Li metal, a buffer layer containing eutectic salts (for example, $NaNO_3$ (33.3 w%)/KNO_3 (66.7 w%)), a solid-state electrolyte, and a metal oxide-based oxygen positive electrode with eutectic salts. The molten-salt Na–O_2 battery has a liquid Na metal negative electrode, solid-state electrolyte, and metal oxide-based oxygen positive electrode with eutectic salts (for example, $NaNO_3$ (26.4 w%)/KNO_3 (27.3 w%)/$CsNO_3$ (46.3 w%) in Fig. S5, ESI†). (c) The comparison of energy and power densities based on the area of the positive electrode in a Ragone plot for alkali metal–oxygen batteries (Li–O_2,[17,18,35–38] Na–O_2,[39,40] K–O_2[41–43] batteries). Detailed information on the reported performance is shown in Table S1 and Fig. S1 (ESI†).

Experimental

Materials

Nickel metal powder (325 mesh, 99.8%, Fisher Scientific Co. LLC.) was used for electrode preparation. $NaNO_3$ (99.999%, Fisher Scientific Co. LLC.), KNO_3 (99.99%, Fisher Scientific Co. LLC.), $CsNO_3$ (99.99%, Fisher Scientific Co. LLC.), $NaNO_2$ (>97%, Fisher Scientific), NaTFSI (sodium trifluoromethanesulfonimide, 97%, Sigma Aldrich), KTFSI (potassium trifluoromethanesulfonimide, 97%, Sigma Aldrich) were used to prepare the eutectic molten-salt electrolytes and electrodes. Na-β-Al_2O_3 discs (Ionotec Ltd.) were used as Na-ion conductors for molten-salt Na–O_2 batteries. Na_2O_2 (97%, Sigma Aldrich), NaO_2 (Thermo Scientific™), Na_2CO_3 (99.5%, Sigma Aldrich) and K_2CO_3 (99.0%, Sigma Aldrich) were used as standard samples for Raman spectroscopy. Standardized titanium(IV) oxysulfate solution (Aldrich, ~15 wt% in dilute sulfuric acid, 99.99% trace metals basis) was used to quantify Na_2O_2 in discharged electrodes.[28] Hydrochloric acid (0.01 N, VWR) was used for acid–base titration experiments for Na_2O and Na_2O_2 from discharged electrodes.[29,30] A Griess reagent system (Promega) was used for nitrite titration for discharged electrodes.[18]

Preparation of the Ni/$NaNO_3$/KNO_3/$CsNO_3$ electrodes

2 g of Ni powder (325 mesh, 99.8%, Fisher Scientific Co. LLC.) was added into 5 mL of a $NaNO_3$ (26.4 w%)/KNO_3 (27.3 w%)/$CsNO_3$ (46.3 w%) solution (0.25 g mL^{-1} in Deionized water, DIW). Then the above suspension was sonicated for 10 min and transferred into an oven for drying at 453 K for 2 hours.

Next, the composite powder was ground for half an hour and pressed as an electrode (0.2 g and 12.7 mm of diameter) onto stainless steel mesh (120 mesh) with 2 tons of pressure for 1 min in an Ar-filled glove box. These electrodes were transferred into a vacuum Buchi glass oven at 473 K for two days and then stored in an argon-filled glove box. After preparation, there is a small amount of NO_2^- in the Ni/$NaNO_3$/KNO_3/$CsNO_3$ electrodes, which can be attributed to at least one of the following reactions:[31] Ni + $NaNO_3$ → NiO + $NaNO_2$ (ΔG^0 = −128.7 kJ mol^{-1} from thermodynamic data in Table S3, ESI†), Ni + KNO_3 → NiO + KNO_2 (ΔG^0 = −122.8 kJ mol^{-1} from thermodynamic data in Table S3, ESI†) or Ni + $CsNO_3$ → NiO + $CsNO_2$ (ΔG^0 = −118.4kJ mol^{-1} from thermodynamic data in Table S3, ESI†).

Preparation of Ni/NaTFSI/KTFSI electrodes

2 g of Ni powder (325 mesh, 99.8%, Fisher Scientific Co. LLC.) was added into 5 mL of a NaTFSI (31.9 w%)/KTFSI (68.1 w%) solution (0.25 g mL^{-1} in DIW). Then, the above suspension was sonicated for 10 min, transferred into an oven, and dried at 453 K for 2 hours. Next, the composite powder was ground for half an hour and compressed as a 12.7 mm electrode (0.2 g) on stainless steel mesh (120 mesh) with 2 tons of pressure for 1 min in an Ar-filled glove box. These electrodes were transferred into a vacuum Buchi glass oven at 473 K for two days and then stored in an Ar-filled glove box prior to use.

Synthesis of Na_3ONO_2

Na_2O (Fisher Scientific) and $NaNO_2$ (>97%, Fisher Scientific) with a 1 : 1 molar ratio was ground for 20 min, and then 50 mg of the mixture was pressed as a pellet. After that, the pellets were sealed in an air-tight stainless-steel (SS) reactor under an Ar environment. The reactor was put in the oven at 573 K for 20 h. The produced yellow pellet (Na_3ONO_2) was transferred into an Ar-filled glove box for characterization.

Assembly of Na molten-salt cells

All parts of Na–O_2 cells were dried in a vacuum oven at 353 K for 12 h before use. The liquid Na negative electrode and the Ni/salts positive electrode (12.7 mm in diameter) were separated by a piece of β-Al_2O_3 conductor. A schematic structure of the Na molten-salt cell is shown in the inset of Fig. 2a. After assembly, the cells were charged with O_2 or Ar. The charged O_2 or Ar pressure ranged from ∼70 to 280 kPa at room temperature. There was good wetting between liquid Na and β-Al_2O_3 membrane after resting for 2 hours in Na–O_2 cells (Fig. S2, ESI†).

Characterization of the reaction between Na_2O and O_2

10 mg of Na_2O was added to 200 mg of Ni/salt powder (8/5 weight ratio) and then pressed as a pellet under a pressure of 2 tons. After that, the pellet was put into an air-tight cell with 275 kPa of O_2 or Ar at 443 K for 48 h. After the reaction, the pellet was characterized in an air-tight cell using Raman spectroscopy.

Quantification of the solubility of Na_2O_2 in molten salts

The solubility of Na_2O_2 in $NaNO_3$ (26.4 w%)/KNO_3 (27.3 w%)/$CsNO_3$ (46.3 w%) eutectic molten salt was measured *via* an acid–base titration method. 2 w% of Na_2O_2 in the above molten salts was stirred at 443 K for two days, and then rest for three days at the same temperature. After that, the top, clear molten salt was collected for acid–base titration.

Electrochemical measurements

Molten-salts Na–O_2 cells were measured on a temperature-controlled hot plate. The temperature was set at 443 K. The operation voltage window was set between 1.8 to 2.8 V. The applied current density ranged from 0.1 to 10 mA cm^{-2}_{geo}. The battery tests were conducted using a Biologic VMP3 electrochemical workstation. The areal capacity, energy density and power density obtained from the electrochemical measurements were normalized by the area of the positive electrode.

Differential electrochemical mass spectrometry (DEMS) measurements were conducted on a custom-made DEMS setup which has been detailed previously.[32] $^{32}O_2$ ($^{16}O^{16}O$), $^{34}O_2$ ($^{16}O^{18}O$), and $^{36}O_2$ ($^{18}O^{18}O$) were detected during charging with 10 min of accumulation time for each point. O_2 pressure was measured during the discharge process to quantify the O_2 consumption. Helium (Ultra High Purity 5.0 Grade, Airgas) was used as the carrier gas in DEMS measurements. The effective area of electrodes was 0.785 cm^2 for DEMS measurement. The operation temperature was 443 K. The applied discharge and charge current densities ranged from 0.1 to 0.4 mA cm^{-2}_{geo}.

Quantification of discharge products

NO_2^- was quantified using the Griess method.[18] NO_2^- titration was conducted on a UV-vis spectrophotometer (Genesys 180, Thermo Fisher Scientific). The NO_2^- calibration curve was generated using titration of the standard NO_2^- solutions (0, 0.01, 0.02, 0.05, 0.1, 0.5, 1 mM). 50 μL of standard NO_2^- solution and 50 μL of sulfanilic acid (10 mg mL^{-1} solution in 5% phosphoric acid, Promega) were added into a 1.2 mL plate deep well and then was kept in a dark environment for 3–5 min. Next, 50 μL of *N*-(1-naphthyl)ethylenediamine dihydrochloride (1 mg mL^{-1}) solution (Promega) was added to the above solution and was kept in a dark environment for another 3–5 min. After that, 100 μL of the above solution was transferred into a quartz cuvette (10 mm path length, VWR) with 1.9 mL of deionized water (DIW). The solution in the cuvette was tested immediately using UV-vis with a scanning rate of 1 nm s^{-1} from 450 to 700 nm. The curve of absorbance *vs.* NO_2^- concentration was linearly fit, as shown in Fig. S3 (ESI†). For quantification of electrodes, the samples were dispersed in 50 mL of DIW, and then a clear solution was obtained by centrifugation. The clear solution was diluted ranging from 1/50 to 1/100. The diluted solution was then titrated using the above procedure.

Na_2O_2 was quantified using titanium oxysulfate titration. Discharged electrodes were extracted from discharged molten-

salt Na–O_2 or Na–Ar cells in an Ar-filled glove box. Then, the electrode was removed from the glovebox and immediately dispersed in 50 mL of cooled DIW (stored in a refrigerator at 278 K) and stirred for 4 min. During this time, the following reaction occurred: $Na_2O_2 + 2H_2O \rightarrow 2\,NaOH + H_2O_2$. There is a side reaction $Na_2O_2 + H_2O \rightarrow 2NaOH + 0.5O_2$, which can be neglected based on literature findings.[28] Next, 1 mL of the solution was filtered using a 0.2 μm filter and was added to 1 mL of cooled DIW and titrated with 0.5 mL standardized titanium(IV) oxysulfate solution (Aldrich, ~15 wt% in dilute sulfuric acid, 99.99% trace metals basis). This step allows the fast reaction between H_2O_2 and Ti^{4+}oxysulfate to form yellow pertitanic acid. The reaction is $Ti^{4+} + H_2O_2 + 2H_2O \rightarrow H_2TiO_4 + 4H^+$. The concentration of the yellow pertitanic acid was determined using UV-vis spectroscopy (Genesys 180, Thermo Fisher Scientific) with a scanning rate of 1 nm s^{-1} from 350 to 650 nm. The UV-vis spectra of the titration of standardized H_2O_2 solutions (Certified ACS 31.7%, Fisher Chemical) at various concentrations (0.08, 0.2, 0.4, 0.8, 1.2, 1.6 mM) and the corresponding calibration curve are shown in Fig. S4 (ESI†).

Acid–based titrations for Na_2O quantification were done using a pH meter (PH 700 meter, VWR) and 0.01 N of HCl standard solution (VWR). All discharged electrodes were first dispersed in 20 mL of DIW, and then clear solutions were collected *via* centrifugation and filtration using a 0.2 μm filter. The reaction of Na_2O in the electrode and DIW is $Na_2O + H_2O$ = 2NaOH.[22] 1 mL of the filtered solution was diluted to 10 ml for acid–base titration. The titration reaction is NaOH + HCl = NaCl + H_2O.[21] The end point of the titration was determined by the pH reaching ~7 (6.5–7.5). In the event that Na_2O_2 was detected, the contribution from Na_2O_2 was deducted from the value determined from acid–base titration to determine the contribution from Na_2O.

Characterization of electrodes

Ni electrodes were characterized through X-ray diffraction (XRD, Bruker D2), scanning electronic microscopy (SEM, Zeiss Merlin), and Raman spectroscopy (HORIBA Scientific LabRAM HR800). In the measurements of XRD and Raman spectra, the electrodes were sealed in air-tight cells. In XRD measurements, the applied voltage and current were 30 kV and 10 mA, respectively, using Cu-Kα radiation (λ = 1.54178Å). In Raman spectroscopy measurements, a red laser (λ = 632.8 nm) was used with 50-fold magnification. An exposure time of 15 s with a 600 grating was used, and each spectrum was accumulated five times.

Results and discussion

Electrochemical performance of molten-salt Na–O_2 cells

Molten-salt Na–O_2 cells discharged at 443 K exhibited discharge voltages of 1.9–2.1 V at rates up to 10 mA cm^{-2}_{geo}, where the cells consisted of a liquid Na negative electrode, β-Al_2O_3 membrane and Ni/$NaNO_3$/KNO_3/$CsNO_3$/stainless steel (SS) oxygen electrode (inset of Fig. 2a). A ternary $NaNO_3$ (26.4 w%)/KNO_3 (27.3 w%)/$CsNO_3$ (46.3 w%) eutectic molten-salt electrolyte was selected due to its lower melting temperature (427 K in Fig. S5, ESI†) compared to $NaNO_3$/KNO_3 (494 K) and $NaNO_3$/$CsNO_3$ (464 K) binary eutectics (Table S2, ESI†). Critically, all three nitrate salts show thermal stability up to 600 K,[33] which is significantly higher than the operating temperature of 443 K in this study. By investigating different weight ratios of Ni to $NaNO_3$/KNO_3/$CsNO_3$ salts, an optimal ratio of 8/5 was identified, which yielded a discharge capacity of ~16 mA h cm^{-2}_{geo} at 0.2 mA cm^{-2}_{geo} (Fig. S6, ESI†). Increasing current density from 0.2 to 10 mA cm^{-2}_{geo} was accompanied by an exponential decrease in areal capacity suggesting that the discharge process could be limited by O_2 diffusion at high rates (Fig. 2a and Fig. S7, ESI†). On the other hand, the discharge voltages decreased linearly with increasing current densities in Fig. 2a and Fig. S7 (ESI†), which was consistent with the overpotential being governed by the cell's resistance of ~10 Ω from the slope in Fig. S7 (ESI†). Further support came from electrochemical impedance spectroscopy (EIS) in Fig. S8 (ESI†) which revealed low Ohmic resistance (R1) of ~7 Ω, charge transfer resistance

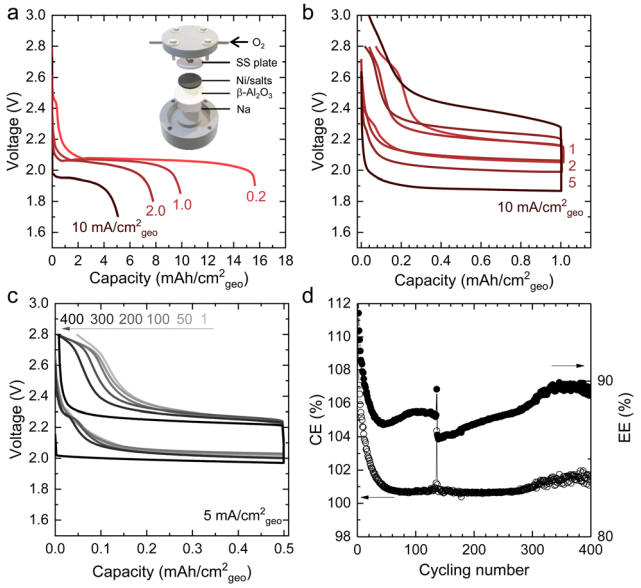

Fig. 2 The electrochemical performance of molten-salt Na–O_2 batteries. (a) Discharge profiles of molten-salt Na–O_2 batteries at different current densities (0.2, 1.0, 2.0, 10.0 mA cm^{-2}_{geo}). The inset of (a) is the schematic structure of a molten-salt Na–O_2 battery, including liquid Na negative electrode, β-Al_2O_3 membrane, Ni/$NaNO_3$/KNO_3/$CsNO_3$/SS positive electrode, stainless steel (SS) mesh current collector, and O_2. (b) Charge-discharge profiles of molten-salt Na–O_2 batteries at different current densities (1, 2, 5, 10 mA cm^{-2}_{geo}) with a limited discharge capacity of 1.0 mA h cm^{-2}_{geo} (~6% depth of discharge based on 16 mA h cm^{-2}_{geo} in (a)). (c) Charge–discharge profiles of a molten-salt Na–O_2 battery at a current density of 5 mA cm^{-2}_{geo} (1st, 50th, 100th, 200th, 300th, and 400th cycles) with a limited discharge capacity of 0.5 mA h cm^{-2}_{geo} (~3% depth of discharge based on 16 mA h cm^{-2}_{geo} in (a)). Cycling at deeper depths of discharge was limited by the β-Al_2O_3 membrane. (d) The Coulombic (CE) and energy efficiencies (EE) of a molten-salt Na–O_2 battery at a current density of 5 mA cm^{-2}_{geo} for 400 cycles. All of the above cells were tested at 443 K on a hot plate with thermal insulation, where fluctuations during cycling are attributed to changes in the cell temperature. The molten salt is a mixture of $NaNO_3$ (26.4 w%), KNO_3 (27.3 w%), and $CsNO_3$ (46.3 w%).

between β-Al_2O_3 and the electrodes (R2) of ~8 Ω, and low ionic resistances from β-Al_2O_3 (R3) of ~2 Ω. These resistances add up to a total cell resistance of ~17 Ω which is similar in magnitude to the slope of discharge voltage *vs.* current from Fig. S7 (ESI†) (~10 Ω). Moreover, galvanostatic intermittent titration technique (GITT) measurements in Fig. S9a (ESI†), showed small overpotentials (<10 mV, the inset of Fig. S9a, ESI†) for the discharge plateau, with 3–4 mV of the overpotentials came from charge/discharge iR drop (Fig. S9, ESI†). Remarkably, these results suggest fast oxygen redox kinetics in molten-salt Na–O_2 cells in contrast to reported room temperature Na–O_2 batteries using organic aprotic solvents for the electrolytes and carbon nanotube electrodes[34] which had a discharge overpotential of ~1 V at a rate of 1 mA cm^{-2}_{geo}.

Molten-salt Na–O_2 cells also demonstrated low overpotentials during charging, as well as high cycling stability (400 cycles), and high Coulombic (~100% at 5 mA cm^{-2}_{geo}) and energy (~90% at 5 mA cm^{-2}_{geo}) efficiencies. Molten-salt Na–O_2 cells were discharged and charged with capacities limited to 1 mA h cm^{-2}_{geo} at rates from 1 mA cm^{-2}_{geo} to 10 mA cm^{-2}_{geo} (Fig. 2b). Remarkably, even at high rates of 10 mA cm^{-2}_{geo}, the overpotential on charge remained small (<300 mV) for most of the charging process, only increasing sharply after 0.8 mA h cm^{-2}_{geo}. Moreover, molten-salt Na–O_2 cells could be stably cycled at 5 mA cm^{-2}_{geo} to 0.5 mA h cm^{-2}_{geo} for 400 cycles (Fig. 2c) with negligible increase in overpotential, as well as stable Coulombic (CE) and energy efficiencies (EE) of ~100% and ~90%, respectively (Fig. 2d). Moreover, increasing the cut-off capacity during cycling to 1.0 mA h cm^{-2}_{geo}, the molten-salt Na–O_2 cell still showed low overpotentials, long cycling life (100 cycles), and high CE (~100%) and EE (~90%) (Fig. S10, ESI†). Such molten-salt Na–O_2 cells exhibited higher energy (33 mW h cm^{-2}_{geo}) and power densities (19 mW cm^{-2}_{geo}) as compared with even the highest performing nonaqueous Na–O_2 cells with 24 mW h cm^{-2}_{geo} and 1.0 mW cm^{-2}_{geo}.[40] Significantly, when compared to reported Li–O_2 batteries,[18,36] these molten-salt Na–O_2 cells can also provide comparable areal energy density (33 mW h cm^{-2}_{geo} *vs.* 30 mW h cm^{-2}_{geo}[18]) and higher areal power density (19 mW cm^{-2}_{geo} *vs.* 6 mW cm^{-2}_{geo}[36]) than the highest performing cells reported to date. Please see Fig. 1c, Fig. S1, and Table S1 (ESI†) for a detailed comparison of the reported performance of alkali metal–oxygen batteries *vs.* the molten-salt Na–O_2 cells reported in this work.

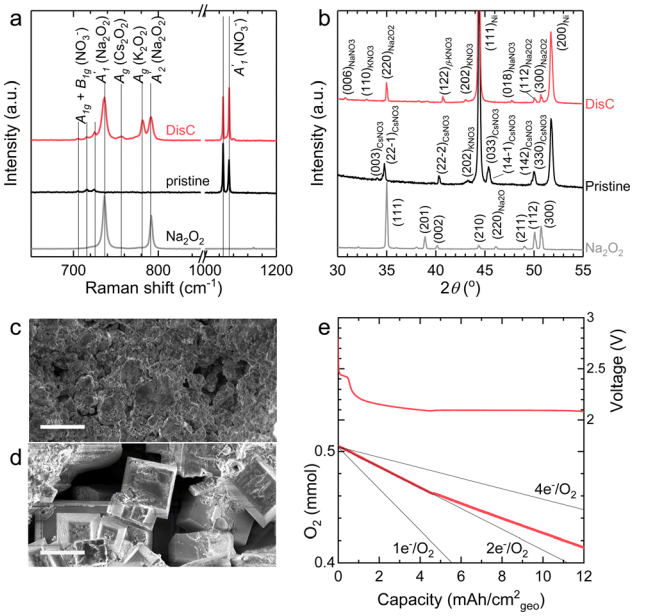

Fig. 3 Characterization of Ni/$NaNO_3$/KNO_3/$CsNO_3$/SS electrodes before and after discharge in molten-salt Na–O_2 batteries. (a) The Raman spectra of Ni/$NaNO_3$/KNO_3/$CsNO_3$/SS electrodes before and after discharge. Raman spectra of commercial Na_2O_2, $NaNO_3$, KNO_3, $CsNO_3$ and prepared eutectic salts (Na/K/$CsNO_3$) were used as the references (Fig. S14, ESI†). (b) The XRD patterns of Ni/$NaNO_3$/KNO_3/$CsNO_3$/SS electrodes before and after discharge and that of commercial Na_2O_2 powder. Several standard XRD patterns of $NaNO_3$ (#01-085-1466), KNO_3 (#04-016-8139), $CsNO_3$ (#04-012-0763), and Na_2O_2 (#01-074-0895) are references. β-KNO_3 was formed in the quenching process[46] and its XRD is from Materials Project.[47] The discharged electrode was washed using dimethyl sulfoxide (DMSO) and then acetonitrile (AN) for the characterization of Raman spectra and XRD. (c and d) The morphology of pristine (c) and discharged (d) electrodes at current of 1 mA cm^{-2}_{geo} for ~10 mA h cm^{-2}_{geo} (Fig. 2a). The scale bars in SEM images are 10 μm. (e) O_2 pressure tracking during discharge of a molten-salt Na–O_2 battery. The black lines represent the oxygen consumption with 1, 2, and 4 electrons per oxygen (e^-/O_2) processes. The effective geometric area of the Ni/$NaNO_3$/KNO_3/$CsNO_3$/SS electrode in this measurement is 0.5 cm^2.

Discharge products of molten-salt Na–O_2 cells

The discharge of molten-salt Na–O_2 cells mainly produces Na_2O_2. Discharge of Ni/$NaNO_3$/KNO_3/$CsNO_3$/SS electrodes was accompanied by the emergence of four Raman bands from 700 to 800 cm^{-1}, which can be assigned to the O–O stretching vibration (Fig. 3a). For instance, the Raman bands at 737 and 792 cm^{-1} are consistent with those reported for the A_1' and A_2' vibration modes of Na_2O_2,[44] while those at 756 and 781 cm^{-1} can be attributed to O–O stretching of Cs_2O_2 (A_g mode)[45] and K_2O_2 (A_g mode),[44] respectively. The presence of K_2O_2 and Cs_2O_2 was unexpected because it is thermodynamically uphill to replace the Na^+ ions in Na_2O_2 with K^+ ($Na_2O_2 + 2KNO_3 \rightarrow K_2O_2 + 2NaNO_3$, ΔG = 75.1 kJ mol^{-1}) or Cs^+ ($Na_2O_2 + 2CsNO_3 \rightarrow Cs_2O_2 + 2NaNO_3$, ΔG = 199.7 kJ mol^{-1}) from the molten nitrate electrolyte (please see ESI† for calculation details). We therefore hypothesize that the K_2O_2 and Cs_2O_2 observed in the discharged electrode came from soluble O_2^{2-} in the molten-salt electrolyte that, upon cooling of the electrodes, became kinetically trapped out of equilibrium. This hypothesis is in agreement with the Raman spectra of an electrode that was cooled slowly (~1 K min^{-1}), which shows very weak Raman bands for K_2O_2 and Cs_2O_2 (Fig. S11, ESI†). Interestingly, Raman spectra of discharged electrodes that had not been washed in aprotic solvents between discharge and characterization (Fig. S12, ESI†) showed evidence of some Na_2O formation, which will be discussed below. Further support that the dominant discharge product was Na_2O_2 came from XRD patterns of washed, discharged electrodes (Fig. 3b) that showed clear peaks from Na_2O_2 ((220), (112), and (300)), but none from K_2O_2 or Cs_2O_2 or

Na_2O, where small amounts of amorphous Cs_2O_2 and K_2O_2 formed during cooling of the electrode would not be detectable using XRD. SEM images (Fig. 3c and d) reveal Na_2O_2 large faceted crystals (5 to 30 μm) produced in the discharged electrode, which may be attributed to the high solubility of Na_2O_2 (65 mM, detailed method in ESI†) in $NaNO_3/KNO_3/CsNO_3$ molten-salts.

The formation of Na_2O_2, as well as some Na_2O during discharge of molten-salt Na–O_2 cells is further supported by the equilibrium potential from cyclic voltammogram (CV) measurements as well as pressure tracking and titration measurements. CVs collected using a molten-salt Na–O_2 cell at 0.2 mV s^{-1} (Fig. S13, ESI†) showed a cathodic peak at 2.00 V, and anodic peak at 2.26 V. Significantly, the equilibrium potential estimated by $E_{1/2}$ was 2.12 V, which is similar to that obtained from GITT measurements ~2.09 V (Fig. S9a, ESI†), as well as the calculated thermodynamic potential of the $2Na^+ + O_2 + 2e^- \rightarrow Na_2O_2$ at 443 K (2.15 V_{Na}, see ESI† for details), but different from the formation NaO_2 (2.07 V_{Na}, see ESI† for details) and Na_2O (1.86 V_{Na}, see ESI† for details), in agreement with the overall reaction being the formation of Na_2O_2 from O_2. Interestingly, pressure tracking measurements (Fig. 3e) of molten-salt Na–O_2 cells during discharge showed two distinct regions corresponding to a 2.0 e^-/O_2 process at early discharge (0–4.5 mA h cm^{-2}_{geo}) and a 2.8 e^-/O_2 process later in discharge (4.5–12 mA h cm^{-2}_{geo}). The transition between the 2.0 e^-/O_2 and 2.8 e^-/O_2 processes at a discharge capacity of ~4.5 mA h cm^{-2}_{geo} was accompanied by a transition from a sloped discharge voltage profile to a flat voltage profile once the discharge voltage reached ~2.10 V. While the 2.0 e^-/O_2 in early discharge is consistent with the formation of Na_2O_2, the 2.8 e^-/O_2 process later in discharges suggests the formation of both Na_2O_2 (2 e^-/O_2) and Na_2O (4 e^-/O_2). The origin of these two regions during cell discharge will be discussed later. Further evidence that the discharge product contained both Na_2O_2 and Na_2O came from quantifications of a $Ni/NaNO_3/KNO_3/CsNO_3$/SS electrode discharged to 6.0 mA h cm^{-2}_{geo} *via* the Griess method[18] (Fig. S3, ESI†), Ti(IV) oxysulfate[16] (Fig. S4, ESI†), and acid–based titrations[29] (details in the Experimental section). As shown in Fig. 4a, the pristine $Ni/NaNO_3/KNO_3/CsNO_3$/SS electrode showed only a small amount of NO_2^- (11.7 μmol), which may come from a chemical reaction between Ni and nitrate salts (please see details in the Experimental section), but no Na_2O_2 and Na_2O. On the other hand, following discharge, there was no NO_2^-, but instead 22.2 μmol of Na_2O and 99.9 μmol of Na_2O_2 were detected, which combined, accounts for 5.2 mA h cm^{-2}_{geo} comparable to the actual capacity of 6.0 mA h cm^{-2}_{geo}. The mechanism for the formation of both Na_2O_2 and Na_2O will be discussed later in detail.

Nitrate anions are redox active in molten-salt Na–O_2 batteries

Discharging $Ni/NaNO_3/KNO_3/CsNO_3$/SS electrodes in Na–Ar cells resulted in the formation of Na_3ONO_2 (from equimolar Na_2O and $NaNO_2$) with a discharge voltage of ~1.6 V (Fig. S15 and S16, ESI†). $Ni/NaNO_3/KNO_3/CsNO_3$/SS electrodes could be discharged to capacities of >12 mA h cm^{-2}_{geo} in Na–Ar cells

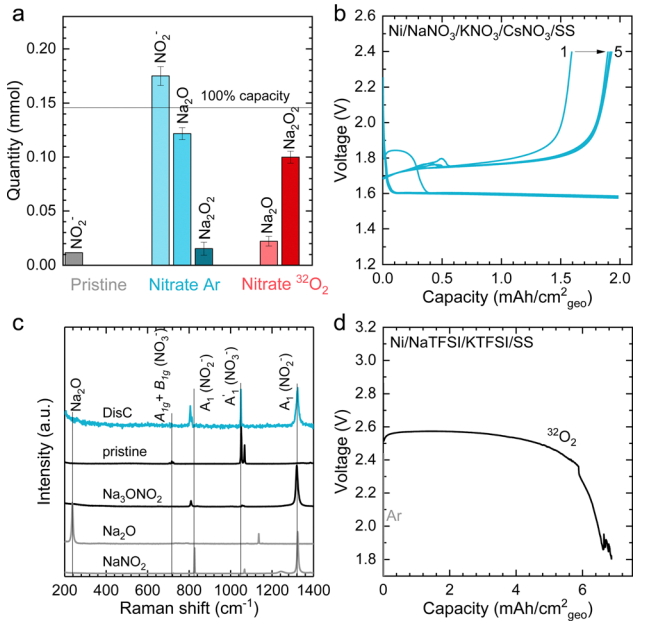

Fig. 4 The electrochemical performance and characterization of molten-salt Na–Ar batteries. (a) Titration results of pristine and discharged $Ni/NaNO_3/KNO_3/CsNO_3$/SS electrodes in O_2 and Ar (see Fig. S15, ESI† for the discharge profiles of the electrode). The amounts of NO_2^- measured *via* the Griess method (Fig. S3, ESI†),[18] Na_2O *via* the acid–base method,[29] and Na_2O_2 *via* the titanium oxysulfate titration method (Fig. S4, ESI†).[16] The pristine electrode showed a small amount of NO_2^-, which was attributed to the electrode preparation process (see Experimental section for details). (b) The charge–discharge profiles of a molten-salt Na–Ar cell at a current density of 1 mA cm^{-2}_{geo} (1st to 5th cycles) with a limited discharge capacity of 2.0 mA h cm^{-2}_{geo} at a temperature of 443 K. (c) The Raman spectra of positive electrodes before and after discharge from Na–Ar cells. Raman spectra of commercial Na_2O and $NaNO_2$, as well as synthetic Na_3ONO_2 as a reference (see Experimental section for preparation details). (d) The discharge profiles of molten-salt Na–O_2 cells with eutectic salt of NaTFSI (31.9 w%)/KTFSI (68.1 w%) in $^{32}O_2$ and Ar at current density of 0.2 mA cm^{-2}_{geo} at temperature of 483 K.

(Fig. S17, ESI†). Na–Ar cells with $Ni/NaNO_3/KNO_3/CsNO_3$/SS electrodes could be discharged stably at rates up to 5 mA cm^{-2}_{geo} (Fig. S17, ESI†) and after the first cycle, could be cycled with Coulombic efficiency (CE) of ~104% for 5 cycles (Fig. 4b and Fig. S18, ESI†). Raman spectra of the discharged electrode (Fig. 4c) showed bands at 810, 1056, 1064, 1319 cm^{-1} which are consistent with those of Na_3ONO_2. Na_3ONO_2 is an adduct of equimolar Na_2O and $NaNO_2$, and can be readily formed from the reaction between Na_2O and molten $NaNO_2$ at elevated temperatures[48] (details in the Experimental section). CV measurements of Na–Ar cells (Fig. S19, ESI†) showed a cathodic peak at 1.46 V and anodic peak at 1.89 V, corresponding to an equilibrium potential of ~1.68 V, which is in good agreement with the thermodynamic potential of $NaNO_3 + 2Na^+ + 2e^- \rightarrow Na_2O + NaNO_2$ at 443 K (E° = 1.49 V, see ESI† for details). Further support that the discharge of $Ni/NaNO_3/KNO_3/CsNO_3$/SS electrodes in Na–Ar cells forms equimolar Na_2O and $NaNO_2$ came from titration measurements that showed 175.0 μmol of $NaNO_2$, 121.7 μmol of Na_2O and 15.4 μmol of Na_2O_2 (Fig. 4a), which combined, corresponds to a discharge capacity of

5.77 mA h cm^{-2}_{geo} and is close to the actual capacity of 6.0 mA h cm^{-2}_{geo}. The small amount of Na_2O_2 can be attributed to the direct formation of Na_2O_2 from $NaNO_3$ given by $NaNO_3 + Na^+ + e^- \rightarrow NaNO_2 + 1/2Na_2O_2$ with $E^\circ = 1.44\ V_{Na}$ at 443 K. The redox activity of nitrate anions in molten-salt Na–Ar cells is in agreement with recent work on molten-salt Li–Ar cells.[49]

The presence of redox active nitrate anions in the electrolyte is essential to enable molten-salt Na–O_2 cells that form Na_2O_2 during discharge. Given the observed redox activity of nitrate anions in molten-salt Na–Ar cells, molten-salt cells were constructed where nitrate anions were replaced with redox inactive bis(trifluoromethanesulfonyl)imide anions ($TFSI^-$) by using NaTFSI/KTFSI (31.9/68.1 w%) eutectic salt[50] with a melting temperature of 453 K as the electrolyte. The redox inactivity of $TFSI^-$ anions was confirmed by the negligible capacity of molten-salt Na–Ar cells with Ni/NaTFSI/KTFSI/SS electrodes (Fig. 4d). Molten-salt Na–O_2 cells with Ni/NaTFSI/KTFSI/SS electrodes discharged at 483 K showed a much higher discharge voltage of ~2.6 V (Fig. 4d) compared to Ni/$NaNO_3$/KNO_3/$CsNO_3$/SS electrodes. Significantly, Raman spectra of the discharged Ni/NaTFSI/KTFSI/SS electrode (Fig. S20a, ESI†) indicated the formation of Na_2CO_3 (1080 cm^{-1}, A_1' (CO_3^{2-})) and K_2CO_3 (1055 cm^{-1}, A_1' (CO_3^{2-})), but not Na_2O_2. The formation of Na_2CO_3 and K_2CO_3 could be attributed to the decomposition of the $TFSI^-$ anion, the only major source of carbon in the electrode. Acid–base titration measurements confirmed that negligible amounts of NaO_2, Na_2O_2 or Na_2O were present in discharged Ni/NaTFSI/KTFSI/SS electrodes. The formation of parasitic Na_2CO_3 and K_2CO_3 during the discharge of Ni/$NaNO_3$/KNO_3/$CsNO_3$/SS electrodes is consistent with negligible capacity (<0.03 mA h cm^{-2}_{geo}) upon charging to 3 V (Fig. S20b, ESI†). Through comparison of $NaNO_3$/KNO_3/$CsNO_3$ and NaTFSI/KTFSI electrolytes, it is clear that nitrate anions are critical for highly cyclable molten-salt Na–O_2 batteries. We next examine the chemical reactions between O_2 and the Na_2O and $NaNO_2$ that can form from the electrochemical reduction of NO_3^-.

Chemical oxidation of Na_2O and $NaNO_2$ by O_2

$NaNO_2$ can be oxidized chemically by O_2 to form $NaNO_3$, while Na_2O can react with O_2 to form Na_2O_2 in Ni/$NaNO_3$/KNO_3/$CsNO_3$/SS electrodes. In order to assess the reaction between Na_2O and O_2, Ni/$NaNO_3$/KNO_3/$CsNO_3$/SS electrodes were prepared with added Na_2O, and held at 443 K in both an O_2 and Ar environment for 48 hours. Following 48 hours in an Ar environment, the Raman spectra of the Ni/$NaNO_3$/KNO_3/$CsNO_3$/SS electrode with added Na_2O was largely unchanged, retaining a strong signal at 237 cm^{-1} from Na_2O (Fig. 5a). On the other hand, following the reaction in an O_2 environment, the Raman peak for Na_2O at 237 cm^{-1} disappeared and new Raman peaks at 733 (A_1' (Na_2O_2)), 754 (A_g (Cs_2O_2)), 773 (A_g (K_2O_2)), and 789 cm^{-1} (A_2' (Na_2O_2)) appeared.[44,45] The disappearance of Na_2O and appearance of Na_2O_2 can be attributed to the reaction given by $Na_2O + \frac{1}{2}O_2 \rightarrow Na_2O_2$, which is supported by the fact that Na_2O_2 is thermodynamically more stable than Na_2O and NaO_2 at 443 K, as shown in Fig. 5b. We also noticed that the two

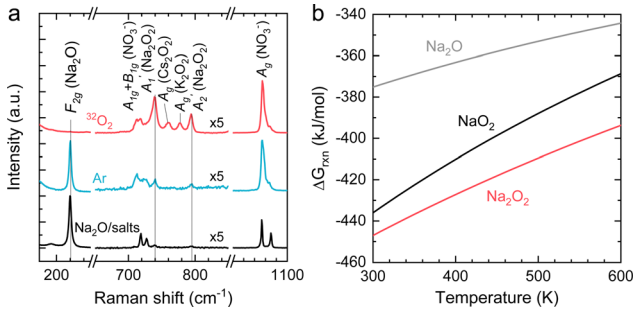

Fig. 5 (a) The Raman spectra of Ni/$NaNO_3$/KNO_3/$CsNO_3$/SS electrodes with the addition of Na_2O before and after reaction in 412 kPa of Ar or $^{32}O_2$ at 443 K. (b) The temperature dependence of the Gibbs free energies for the formation of NaO_2, Na_2O_2, and Na_2O. The Gibbs free energies are calculated based on the following reactions: $2Na + 2O_2 \rightarrow 2NaO_2$, $2Na + O_2 \rightarrow Na_2O_2$ and $2Na + \frac{1}{2}O_2 \rightarrow Na_2O$. Thermodynamic data used for the calculations are given in Table S3 (ESI†).

distinct Raman peaks at 1052 and 1068 cm^{-1} associated with the overlapping A_{1g} modes of KNO_3[51]/$CsNO_3$[52] and the A_{1g} mode of $NaNO_3$,[53] respectively, in the pristine electrode became a single broad peak at 1054 cm^{-1} following the reactions in Ar and O_2, where this change is attributed to the formation of a glassy $NaNO_3$/KNO_3/$CsNO_3$ state[54] following fast cooling of the cell. We further examined the chemicals reactions of Na_2O and $NaNO_2$ with O_2 by exposing a Ni/$NaNO_3$/KNO_3/$CsNO_3$/SS electrode discharged to 7.6 mA h cm^{-2}_{geo} in a He environment, to O_2 at 443 K for 7 hours. Pressure tracking measurements upon the introduction of O_2 showed an initial, very rapid decrease in pressure, following which the pressure slowly stabilized over ~6 hours (Fig. S21, ESI†). By fitting the O_2 consumption curve over the first 3 min we determined a rate of ~0.18 mmol h^{-1}, corresponding to a current density of 25 mA cm^{-2}_{geo} and indicating that the reactions of Na_2O and/or $NaNO_2$ with O_2 can be very fast. This finding is in agreement with previous work[55] that indicates that NO_2^- can be oxidized by O_2 to form NO_3^- in bulk $NaNO_3$/KNO_3 molten salt at temperatures over 573 K.

Nitrate-mediated oxygen reduction reaction in Na–O_2 batteries

The oxygen reduction reaction in molten-salt Na–O_2 batteries occurs *via* a nitrate-mediated mechanism whereby $NaNO_3$ is first reduced electrochemically to form Na_2O and $NaNO_2$ (reaction (1)), following which Na_2O reacts with O_2 to form Na_2O_2 (reaction (2)), and $NaNO_2$ is oxidized by O_2 to regenerate $NaNO_3$ (reaction (3)), resulting in an apparent 2 e^-/O_2 overall reaction given by $2Na^+ + O_2 + 2e^- \rightarrow Na_2O_2$ (reaction (4)). We note in the proposed reaction scheme that nitrate anions are not consumed during discharge such that the entire discharge capacity comes from the overall $2e^-/O_2$ reduction of O_2 to Na_2O_2. Each step of the nitrate-mediated 2 e^-/O_2 reaction has been demonstrated above, where the electrochemical reduction of $NaNO_3$ to Na_2O and $NaNO_2$ was observed in Na–Ar cells (Fig. 4), and the oxidation of Na_2O and $NaNO_2$ by O_2 was shown through chemical experiments (Fig. 5 and Fig. S21, ESI†). Further evidence that the formation of Na_2O_2

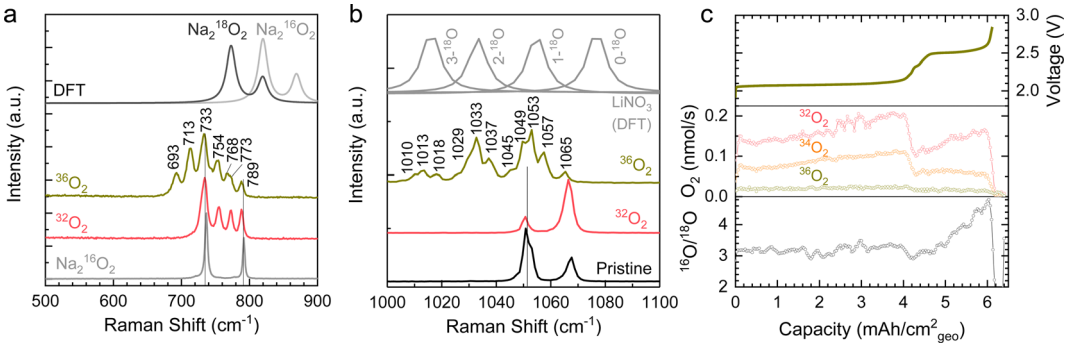

Fig. 6 (a and b) The Raman spectra of discharged Ni/$NaNO_3$/KNO_3/$CsNO_3$/SS electrodes of Na–O_2 cells in $^{36}O_2$ and $^{32}O_2$ and DFT calculated Raman spectra. (c) The rate of oxygen evolution of $^{32}O_2$, $^{34}O_2$, and $^{36}O_2$ as detected by DEMS measurements during charging a symmetric molten-salt Ni/$NaNO_3$/KNO_3/$CsNO_3$/SS battery at 0.2 mA cm^{-2}_{geo} to 2.8 V at 443 K with He carrier gas. Prior to the DEMS measurements, a Na–O_2 cell with Ni/$NaNO_3$/KNO_3/$CsNO_3$/SS was discharged to 8 mA h cm^{-2}_{geo} at 0.2 mA cm^{-2}_{geo} and the positive electrode was collected to serve as the counter electrode for the DEMS measurement. In the DEMS experiments, the battery was kept at OCV for 5 hours at 443 K to ensure full melting of the mixture of $NaNO_3$ (26 w%), KNO_3 (27 w%), and $CsNO_3$ (47 w%). The electrode geometric area was 0.785 cm^2_{geo}. The ratio of $^{16}O/^{18}O$ is ~3 in the first charging plateau at ~2.1 V and the ratio increased in the second charging plateau at 2.5 V. The redox potential of nitrate reduction in Ar was ~1.65 V (*vs.* Na negative electrode) and was used to convert the measured cell potential to the voltage (*vs.* Na negative electrode) scale (Fig. S16, ESI†).

from O_2 is facilitated by nitrate anions comes from ^{18}O-isotopic labelling, where according to the purposed mechanism, discharge of Ni/$NaN^{16}O_3$/$KN^{16}O_3$/$CsN^{16}O_3$/SS electrodes in a $^{36}O_2$ ($^{18}O^{18}O$) environment would proceed *via*:

$$2Na^+ + NaN^{16}O_3 + 2e^- \rightarrow NaN^{16}O_2 + Na_2{}^{16}O \quad (1)$$

$$Na_2{}^{16}O + \tfrac{1}{2}\,{}^{36}O_2 \rightarrow Na_2{}^{16/18}O_2 \quad (2)$$

$$NaN^{16}O_2 + \tfrac{1}{2}\,{}^{36}O_2 \rightarrow NaN^{16/18}O_3 \quad (3)$$

$$\text{Overall reaction: } 2Na^+ + {}^{36}O_2 + 2e^- \xrightarrow{N^{16}O_3^-} Na_2{}^{16/18}O_2 \quad (4)$$

Raman spectroscopy of a Ni/$NaN^{16}O_3$/$KN^{16}O_3$/$CsN^{16}O_3$/SS electrode discharged in a $^{36}O_2$ ($^{18}O^{18}O$) environment showed evidence of red-shifted Raman peaks associated with ^{18}O-enrichment of both $NaNO_3$ (reaction (2)) and Na_2O_2 (reaction (3)). As shown in Fig. 6a, $^{36}O_2$ discharged electrodes showed several new red-shift peaks at 693, 713, and 768 cm^{-1} in the O–O stretching region relative to those of ^{16}O-substituted peroxides at 733, 754, 773, and 789 cm^{-1}, which could be attributed to ^{18}O-substituted peroxides. Such red shifts of ^{18}O-substituted Na_2O_2 are supported by the density functional theory (DFT) computed Raman spectra for $Na_2{}^{18}O_2$ and $Na_2{}^{16}O_2$, where the bands of $Na_2{}^{18}O_2$ are shifted by 46 cm^{-1} relative to $Na_2{}^{16}O_2$ (Fig. 6a). Of significance is to note that while red-shifted Raman bands appeared in the $^{36}O_2$ discharged electrodes, the band at 789 cm^{-1} attributable to $Na_2{}^{16}O_2$ remained, suggesting the discharge product was a mixture of $Na_2{}^{18}O_2$ and $Na_2{}^{16}O_2$. In addition, in the NO_3^- symmetric stretching region, there are also red-shift peaks at 1010, 1013, 1018, 1029, 1033, 1037, 1045, and 1057 cm^{-1}, consistent with the formation of ^{18}O-substituted $NaNO_3$, KNO_3 and $CsNO_3$ (Fig. 6b). Such red shifts in the NO_3^- symmetric stretching region due to ^{18}O-enrichment is supported by simulated wavenumber of symmetric stretching as a function of ^{18}O-substituted-$N^{16}O_3^-$ (Fig. 6b) obtained from DFT calculations of the isolated anion in vacuum at the B3LYP/6-31G(d,p) level, where greater red-shifts in the symmetric stretching were correlated with greater ^{18}O substitution in $N^{16}O_3^-$. The presence of ^{18}O-substituted-$N^{16}O_3^-$ can be attributed to the oxidation of $N^{16}O_2^-$ by $^{36}O_2$ given by reaction (3).

Further evidence of a nitrate-mediated, apparent 2 e^-/O_2 oxygen reduction reaction came from differential electrochemical mass spectroscopy (DEMS) ^{18}O-isotopic labelling experiments that showed that evolved oxygen came primarily from nitrate anions, as opposed to the O_2 discharge environment. DEMS measurements were conducted using a symmetric molten-salt Na–O_2 cell discharged in $^{36}O_2$ (Fig. 6c). The negative electrode used in the DEMS cell was prepared in a Na–Ar cell with discharge capacity of 1.6 mA h cm^{-2}_{geo} to achieve a flat discharge plateau (Fig. S16, ESI†). Upon charging at 0.2 mA cm^{-2}_{geo}, three types of molecular oxygen (*i.e.*, $^{32}O_2$ ($^{16}O^{16}O$), $^{34}O_2$ ($^{16}O^{18}O$), and $^{36}O_2$ ($^{18}O^{18}O$)) were detected, consistent with the decomposition of $Na_2{}^{16}O^{16}O$, $Na_2{}^{16}O^{18}O$ and $Na_2{}^{18}O^{18}O$, respectively. Remarkably, the amount of $^{36}O_2$ evolved was very small (<2%), which indicates only a small amount of $Na_2{}^{18}O^{18}O$ was formed during discharge in $^{36}O_2$, consistent with a nitrate-mediated reaction, as opposed to the direct reduction of O_2 to Na_2O_2. The high proportion (90%) of $^{32}O_2$ ($^{16}O^{16}O$) detected during charge is in disagreement with reactions (1)–(4), which can be attributed to either (1) that the electrochemical reduction of $NaNO_3$ to Na_2O_2 given by $NaNO_3 + Na^+ + e^- \rightarrow NaNO_2 + 1/2Na_2O_2$ can contribute more significantly to the discharge process in Na–O_2 cells as opposed to that observed in Na–Ar cells in Fig. 4a, (2) that the lower O_2 pressure for $^{36}O_2$ cells ~100 kPa as opposed to $^{32}O_2$ cells ~410 kPa slowed reactions (2) and (3), resulting in a higher proportion of $Na_2{}^{16}O$ in the discharged electrode, which could evolve $^{32}O_2$ ($^{16}O^{16}O$) or (3) that the nitrate-mediated reaction pathway is more complex than that given by reactions (1)–(4). Although this discrepancy motivates additional research into the detailed mechanism, we note that the high ratio of $^{16}O/^{18}O$ ~3 in

Fig. 6c strongly supports the hypothesis of a nitrate-mediated oxygen reduction reaction instead of direct O_2 reduction in molten-salt Na–O_2 cells.

In this work, we have reported a molten-salt Na–O_2 battery where the formation of Na_2O_2 is mediated by the electrochemical activity of nitrate anions. Such findings are similar to our recent work on molten-salt Li–O_2 batteries[19] where the redox activity of nitrate anions can enable the formation of Li_2O upon discharge at 423 K. However, in molten-salt Li–O_2 cells, the Li_2O formed from the reduction of NO_3^- to NO_2^- is thermodynamically preferred to Li_2O_2,[18] whereas in Na–O_2 cells, Na_2O can further react with O_2 to form Na_2O_2. The mediation of the oxygen reduction reaction by nitrate anions in molten-salt Li–O_2 and Na–O_2 cells has a number of interesting implications on the cell design and performance. First, the catalytic activity of the electrode surface towards nitrate redox is critical to enable high rates and low overpotentials. In molten-salt Li–O_2 cells, we identified NiO as having high catalytic activity due to its optimum binding of NO_3^- and NO_2^-, where weaker binding catalysts like Cu_2O were limited by NO_3^- adsorption whereas stronger binding catalysts like Mn_3O_4 were limited by the oxidation of NO_2^- by O_2.[19] The high performance of Ni-based catalysts for nitrate redox is in agreement with previous reports for Li–Ar cells.[19,49] Second, the high weight of Ni-based electrodes limits the achievable specific energy of the positive electrode,[18,19] necessitating the development of novel electrode materials with high catalytic activity for nitrate redox with lower weight, such as Ni-coated carbon.[18] Third, while the electrolyte is not consumed in the overall reaction where nitrate anions can participate in multiple catalytic cycles over the span of a single discharge (reactions (1)–(3)), the role of nitrate's redox activity in the oxygen reduction reaction may introduce limitations in the lean-electrolyte regime needed to achieve high cell level specific energy, warranting additional research. Fourth, the blocking of O_2 within the electrode due to accumulation of the discharge product may shift the discharge product towards the formation of Na_2O at deeper discharges, which may be responsible for the presence of minor Na_2O in addition to major Na_2O_2 in deep discharge observed in Fig. 3e. Finally, the temporary formation of NO_2^- in the electrolyte during discharge may locally alter the physicochemical properties of the molten-salt electrolyte, such as its melting point, viscosity or ionic conductivity. During charging, our recent work[56] has shown that the 2 electron oxidation of bulk Na_2O_2 to O_2 is limited by the last step ($NaO_2 \rightarrow O_2 + Na^+ + e^-$), which is known to occur with small overpotentials in Na–O_2 cells with aprotic solvents,[39] rationalizing the small charging overpotentials observed in this work. However, further work is needed to confirm the reaction pathway upon charging in molten-salt Na–O_2 batteries. While this work has shown that molten-salt Na–O_2 batteries can achieve promising areal energy (33 mW h cm^{-2}_{geo}) and power densities (19 mW cm^{-2}_{geo}) as well as stable cycling (400 cycles) and high energy efficiencies $\sim$90%, further research efforts are needed to achieve commercially viable cell level performance.

Conclusions

In summary, we report high-performance molten-salt Na–O_2 batteries with a simple structure, utilizing a nitrate-mediated reaction to achieve $>2e^-/O_2$. First, we investigated the electrochemical performance of these molten-salt Na–O_2 batteries, showing high power density (19 mW cm^{-2}_{geo}) at 10 mA cm^{-2}_{geo} and high-energy efficiency ($\sim$90%) at a high current density of 5 mA cm^{-2}_{geo}, with long cycle life (400 cycles). Next, using Raman, pressure tracking and titration measurements, we showed that the dominant discharge product was Na_2O_2. We further studied the redox activity of nitrate anions in Na–Ar cells, showing that $NaNO_3$ could be electrochemically reduced to Na_2O and $NaNO_2$, where Na_2O and $NaNO_2$ could further react chemically with O_2. Finally, using ^{18}O-labeling experiments, we showed that the oxygen reduction reaction in molten-salt Na–O_2 batteries occurred *via* a nitrate-mediated mechanism whereby $NaNO_3$ was first electrochemically reduced to form Na_2O and $NaNO_2$, following which Na_2O reacted with O_2 to form Na_2O_2, while $NaNO_2$ was oxidized by O_2 to regenerate $NaNO_3$, resulting in an apparent 2 e^-/O_2 overall reaction to form Na_2O_2. Such nitrate-mediated molten-salt Na–O_2 batteries provide a novel approach to develop alkali metal–O_2 batteries with high energy and power density.

Author contributions

Y. G. Z., G. L. and Y. S. H. conceived and designed the study. Y. G. Z., G. L., A. A., K. G., Y. Z. and Y. S. H. conducted experiments, computation, and analysis. Y. G. Z., G. L. and Y. S. H. wrote the manuscript, and all authors edited the manuscript. There is no competing interest. All data and materials used in the work are available in the manuscript or supplementary materials.

Conflicts of interest

Y. G. Z., G. L. and Y. S. H. have applied for a patent related to this work.

Acknowledgements

This work is in part supported by Shell and Department of Navy award N00014-20-1-2221 issued by the Office of Naval Research. The United States Government has a royalty-free license throughout the world in all copyrightable material contained herein. This work made use of the MRSEC Shared Experimental Facilities at MIT, supported by the National Science Foundation under award number DMR-1419807. G. L. gratefully acknowledges partial support from a Natural Sciences and Engineering Research Council of Canada (NSERC) PGS-D and Siebel Scholarship (Class of 2020). We would like to thank Dr Shuting Feng for assistance with DFT calculations.

Notes and references

1 S. J. Davis, N. S. Lewis, M. Shaner, S. Aggarwal, D. Arent, I. L. Azevedo, S. M. Benson, T. Bradley, J. Brouwer and Y.-M. Chiang, *Science*, 2018, **360**, eaas9793.
2 H. Liu, X.-B. Cheng, Z. Jin, R. Zhang, G. Wang, L.-Q. Chen, Q.-B. Liu, J.-Q. Huang and Q. Zhang, *EnergyChem*, 2019, **1**, 100003.
3 H. Wang, D. Yu, C. Kuang, L. Cheng, W. Li, X. Feng, Z. Zhang, X. Zhang and Y. Zhang, *Chemistry*, 2019, **5**, 313–338.
4 J. Xie, L. Liao, Y. Gong, Y. Li, F. Shi, A. Pei, J. Sun, R. Zhang, B. Kong and R. Subbaraman, *Sci. Adv.*, 2017, **3**, eaao3170.
5 D. Lin, Y. Liu and Y. Cui, *Nat. Nanotechnol.*, 2017, **12**, 194.
6 Y.-C. Lu, B. M. Gallant, D. G. Kwabi, J. R. Harding, R. R. Mitchell, M. S. Whittingham and Y. Shao-Horn, *Energy Environ. Sci.*, 2013, **6**, 750–768.
7 J. Read, K. Mutolo, M. Ervin, W. Behl, J. Wolfenstine, A. Driedger and D. Foster, *J. Electrochem. Soc.*, 2003, **150**, A1351–A1356.
8 W. T. Hong, M. Risch, K. A. Stoerzinger, A. Grimaud, J. Suntivich and Y. Shao-Horn, *Energy Environ. Sci.*, 2015, **8**, 1404–1427.
9 D. Aurbach, B. D. McCloskey, L. F. Nazar and P. G. Bruce, *Nat. Energy*, 2016, **1**, 16128.
10 Y.-C. Lu, H. A. Gasteiger and Y. Shao-Horn, *J. Am. Chem. Soc.*, 2011, **133**, 19048–19051.
11 G. V. Chase, S. Zecevic, T. W. Wesley, J. Uddin, K. A. Sasaki, V. P. Giordani, V. Bryantsev, M. Blanco and D. Addison, *US Pat.*, 20120028137, 2012.
12 Y. Chen, S. A. Freunberger, Z. Peng, O. Fontaine and P. G. Bruce, *Nat. Chem.*, 2013, **5**, 489–494.
13 M. M. Ottakam Thotiyl, S. A. Freunberger, Z. Peng and P. G. Bruce, *J. Am. Chem. Soc.*, 2012, **135**, 494–500.
14 Y. G. Zhu, F. T. Goh, R. Yan, S. Wu, S. Adams and Q. Wang, *Phys. Chem. Chem. Phys.*, 2018, **20**, 27930–27936.
15 B. McCloskey, D. Bethune, R. Shelby, G. Girishkumar and A. Luntz, *J. Phys. Chem. Lett.*, 2011, **2**, 1161–1166.
16 S. Feng, M. Huang, J. R. Lamb, W. Zhang, R. Tatara, Y. Zhang, Y. G. Zhu, C. F. Perkinson, J. A. Johnson and Y. Shao-Horn, *Chemistry*, 2019, **5**, 2630–2641.
17 V. Giordani, D. Tozier, H. Tan, C. M. Burke, B. M. Gallant, J. Uddin, J. R. Greer, B. D. McCloskey, G. V. Chase and D. Addison, *J. Am. Chem. Soc.*, 2016, **138**, 2656–2663.
18 C. Xia, C. Y. Kwok and L. F. Nazar, *Science*, 2018, **361**, 777–781.
19 D. Koo and S. J. Kang, *ACS Appl. Mater. Interfaces*, 2021, **13**, 47740–47748.
20 Y. G. Zhu, G. Leverick, L. Giordano, S. Feng, Y. Zhang, Y. Yu, R. Tatara, J. R. Lunger and Y. Shao-Horn, *Joule*, 2022, **6**(8), 1887–1903.
21 K. Baek, J. G. Lee, A. Cha, J. Lee, K. An and S. J. Kang, *J. Power Sources*, 2018, **402**, 68–74.
22 C. Peng, C. Guan, J. Lin, S. Zhang, H. Bao, Y. Wang, G. Xiao, G. Z. Chen and J. Q. Wang, *ChemSusChem*, 2018, **11**, 1880–1886.
23 S. Zhang, Y. Yang, L. Cheng, J. Sun, X. Wang, P. Nan, C. Xie, H. Yu, Y. Xia and B. Ge, *Energy Storage Mater.*, 2021, **35**, 142–147.
24 S. Liu, W. Han, B. Cui, X. Liu, F. Zhao, J. Stuart and S. Licht, *J. Power Sources*, 2017, **342**, 435–441.
25 M. Shahabi, N. Masse, H. Sun, L. Wallace, A. Powell and Y. Zhong, in *REWAS 2022: Energy Technologies and CO2 Management (Volume II)*, Springer; 2022, pp. 47–57.
26 S. Xia, X. Wu, Z. Zhang, Y. Cui and W. Liu, *Chemistry*, 2019, **5**, 753–785.
27 X. Guo, L. Zhang, Y. Ding, J. B. Goodenough and G. Yu, *Energy Environ. Sci.*, 2019, **12**, 2605–2619.
28 B. D. McCloskey, A. Valery, A. C. Luntz, S. R. Gowda, G. M. Wallraff, J. M. Garcia, T. Mori and L. E. Krupp, *J. Phys. Chem. Lett.*, 2013, **4**, 2989–2993.
29 L. S. Darken and H. F. Meier, *J. Am. Chem. Soc.*, 1942, **64**, 621–623.
30 J. Berkowitz, D. J. Meschi and W. A. Chupka, *J. Chem. Phys.*, 1960, **33**, 533–540.
31 P. D. Hooker and K. J. Klabunde, *Chem. Mater.*, 1993, **5**, 1089–1093.
32 J. R. Harding, PhD thesis, Massachusetts Institute of Technology, 2015.
33 K. H. Stern, *J. Phys. Chem. Ref. Data*, 1972, **1**, 747–772.
34 N. Ortiz-Vitoriano, T. P. Batcho, D. G. Kwabi, B. Han, N. Pour, K. P. C. Yao, C. V. Thompson and Y. Shao-Horn, *J. Phys. Chem. Lett.*, 2015, **6**, 2636–2643.
35 X. Gao, Y. Chen, L. Johnson and P. G. Bruce, *Nat. Mater.*, 2016, **15**, 882–888.
36 Z. Peng, S. A. Freunberger, Y. Chen and P. G. Bruce, *Science*, 2012, **337**, 563–566.
37 Z. Zhu, A. Kushima, Z. Yin, L. Qi, K. Amine, J. Lu and J. Li, *Nat. Energy*, 2016, **1**, 16111.
38 Y. Qiao, K. Jiang, H. Deng and H. Zhou, *Nat. Catal.*, 2019, **2**, 1035–1044.
39 P. Hartmann, C. L. Bender, M. Vračar, A. K. Dürr, A. Garsuch, J. Janek and P. Adelhelm, *Nat. Mater.*, 2013, **12**, 228–232.
40 H. Yadegari, M. N. Banis, B. Xiao, Q. Sun, X. Li, A. Lushington, B. Wang, R. Li, T.-K. Sham, X. Cui and X. Sun, *Chem. Mater.*, 2015, **27**, 3040–3047.
41 G. Cong, W. Wang, N.-C. Lai, Z. Liang and Y.-C. Lu, *Nat. Mater.*, 2019, **18**, 390–396.
42 W. Wang, N.-C. Lai, Z. Liang, Y. Wang and Y.-C. Lu, *Angew. Chem., Int. Ed.*, 2018, **57**, 5042–5046.
43 X. Ren and Y. Wu, *J. Am. Chem. Soc.*, 2013, **135**, 2923–2926.
44 H. Eysel and S. Thym, *Z. Anorg. Allg. Chem.*, 1975, **411**, 97–102.
45 T. Livneh, A. Band and R. Tenne, *J. Raman Spectrosc.*, 2002, **33**, 675–676.
46 R. Benages-Vilau, T. Calvet, M. A. Cuevas-Diarte and H. A. J. Oonk, *Phase Transitions*, 2016, **89**, 1–20.
47 Persson, Data retrieved from the Materials Project for KNO_3 (mp-5158) from database version v2021.11.10, Materials Project, 2022, DOI: **10.17188/1263112**.
48 M. Jansen, *Angew. Chem., Int. Ed. Engl.*, 1976, **15**, 376–377.
49 V. Giordani, D. Tozier, J. Uddin, H. Tan, B. M. Gallant, B. D. McCloskey, J. R. Greer, G. V. Chase and D. Addison, *Nat. Chem.*, 2019, **11**, 1133–1138.

50 R. Hagiwara, K. Matsumoto, K. Tamaki, T. Nohira and T. Goto, *US Pat.*, 20090212743A1, 2009.
51 R. Carr, J. Vanos and B. H. Torrie, *Chem. Phys. Lett.*, 1979, **65**, 73–76.
52 M. Brooker, *J. Chem. Phys.*, 1973, **59**, 5828–5829.
53 D. Rousseau, R. Miller and G. Leroi, *J. Chem. Phys.*, 1968, **48**, 3409–3413.
54 M. K. Raju, *Presented in part at the Proceedings of the Indian Academy of Sciences-Section A*, 1945.
55 V. A. Sötz, A. Bonk, J. Forstner and T. Bauer, *Thermochim. Acta*, 2019, **678**, 178301.
56 J. R. Lunger, N. Lutz, J. Peng, M. Bajdich and Y. Shao-Horn, *Chem. Mater.*, 2022, **34**, 3872–3881.

